ECS Transactions, 80 (1) 53-69 (2017)
10.1149/08001.0053ecst ©The Electrochemical Society

The Dynamics of Nickelidation for Self-Aligned Contacts to InGaAs Channels

R. Chen[a], Xing Dai,[a,b] K. L. Jungjohann[c], W. M. Mook[c], J. Nogan[c], Cesare Soci,[b] S. A. Dayeh[a,d,e]

[a] Department of Electrical and Computer Engineering, University of California San Diego, La Jolla CA 92093, USA
[b] Division of Physics and Applied Physics, School of Physical and Mathematical Sciences, Nanyang Technological University, 21 Nanyang Link, Singapore 637371
[c] Center for Integrated Nanotechnologies, Sandia National Laboratories, Albuquerque, New Mexico 87185, USA
[d] Material Science and Engineering Program, University of California San Diego, La Jolla CA 92093, USA
[e] Department of NanoEngineering, University of California San Diego, La Jolla CA 92093, USA

The rapid development of ultrascaled III−V compound-semiconductor devices requires the detailed investigation of metal-semiconductor contacts at the nanoscale where crystal orientation, size, and structural phase play dominant roles in device performance. Here, we report comprehensive studies on the solid-state reaction between metal (Ni) and ternary III−V semiconductor ($In_{0.53}Ga_{0.47}As$) nanochannels to reveal their reaction kinetics, dynamics, formed crystal structure, and interfacial properties. We observed size-dependent reaction kinetics that are dominated by Ni surface-diffusion at small channel dimensions. We also employed *in-situ* heating in a transmission electron microscope (TEM) to record and analyze the atomic scale dynamics of contact reactions both in the cross-section and along the nanowire channel directions of InGaAs nanowires. Atomic models and nucleation models were introduced to depict the ledge formation and nucleation events. Deformation theory was applied to calculate the strain-induced shift in band-edge energies at the nickelide/InGaAs interface. These observations pave the way for engineered nanoscale contact to III-V transistors.

Introduction

Semiconductor nanowires (NWs) and Fin structures are promising building blocks for next generation ultrascaled devices for electronic and optoelectronic applications [1, 2]. The detailed understanding of and control over the phase transformation that accompanies the formation of their alloyed contacts for lithography-free, self-aligned gate design can accelerate the development of these ultra-scaled devices [3]. Numerous aspects of nanoscale metallization technology were shown to exhibit significantly different behavior from their bulk counterparts [4, 5]. Up to now, the majority of the studies that explored nanoscale contact metallurgy focused on nanostructures of elemental semiconductors, i.e., Si and Ge NWs [6, 7], however detailed contact reactions

Downloaded on 2018-02-22 to IP 155.69.24.171 address. Redistribution subject to ECS terms of use (see ecsdl.org/site/terms_use) unless CC License in place (see abstract).

have not been uncovered in III–V NW channels at atomic resolution. Even for a single element metal contact (e.g., Ni) with III-V nanowires, this phase transformation involves transition from a binary/ternary compound semiconductor to a ternary/quaternary compound metallic contact, making even the simplest material system quite complicated and challenging to study.

Here, we focus on the narrow band gap, high electron mobility III−V semiconductor, $In_xGa_{1-x}As$, motivated by its potential in sub-10 nm metal-oxide-semiconductor field-effect transistors (MOSFETs) [8]. Ni is an excellent metal contact choice to $In_{0.53}Ga_{0.47}As$ nanowires because it can diffuse at relatively low temperatures (typically 180 – 300°C) into $In_{0.53}Ga_{0.47}As$ nanowires and forms a metallic nickelide ($Ni_xIn_{0.53}Ga_{0.47}As$) phase through a solid-state reaction, analogous to the nickel silicide (NixSi) to Si devices, with a nickelide specific contact resistivity as low as 4×10^{-8} Ω.cm^2 [9]. In planar device geometries, the nickelide reaction starts at □230°C, and the polycrystalline phase is thermally stable up to 450°C [10]. The $Ni_xIn_{0.53}Ga_{0.47}As$ lattice adopts the NiAs (B8) structure with x=2 ($Ni_2In_{0.53}Ga_{0.47}As$) [11, 12] but little is known about the reaction details and size dependency in nanowires. This article reviews our work on the solid-state reaction between Ni and InGaAs nanochannels. We discuss the morphologies of the nickelide phase in InGaAs channels and its reaction kinetics, followed by the *in-situ* heating transmission electron microscopy (TEM) observations of atomic scale dynamics both in the cross-section of InGaAs NWs and along the NW channel directions. Finally we finish with the electrical properties of InGaAs nanochannels with Nickelide contacts.

Morphologies and Kinetics of Nickelidation in InGaAs Channels

In order to study the reaction kinetics and the morphology of the formed nickelide phase, we start with the fabrication of horizontally aligned InGaAs NWs on insulator on Si substrate. The InGaAs on insulator on Si eliminates the substrate influence during the thermally driven nickelidation process and provides electrical isolation for subsequent device fabrication. The fabrication of InGaAs NWs on insulator on Si is accomplished with a novel solid-state wafer bonding approach that we developed in our laboratory [13], and is schematically illustrated in Figure 1.

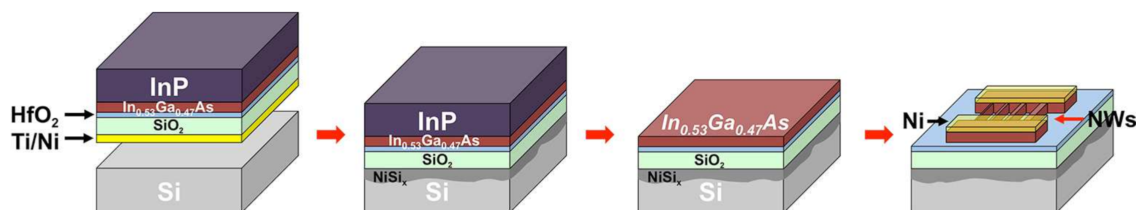

Figure 1. Schematic illustration of the fabrication procedure of horizontally aligned $In_{0.53}Ga_{0.47}As$ nanowire (NW) channels on insulator on Si.

This integration approach utilizes a NiSi reaction under a rapid thermal anneal (RTA), between a top-most Ni layer in a InP/$In_{0.53}Ga_{0.47}As$/dielectrics/Ti/Ni layer stack on an InP substrate and an oxide-free Si carrier wafer. Then, the InP substrate can be removed by lapping and selective wet etching leaving an inverted structure on Si with InGaAs at the

Downloaded on 2018-02-22 to IP 155.69.24.171 address. Redistribution subject to ECS terms of use (see ecsdl.org/site/terms_use) unless CC License in place (see abstract).

surface. The horizontal NW structures are patterned utilizing a 100 kV e-beam writer (JEOL JBX- 6300FS) with a beam size of □10 nm, followed by a Cl-base RIE/ICP dry etching. Next, a 200 nm Ni film is evaporated at the two ends of the Fin structures, and finally the nickelide formation is controlled by RTA in the temperature range from 250 to 300 °C.

Orientation-Dependent Nickelide Morphologies

Figure 2a,b are scanning electron microscope (SEM) images of the Ni contact on InGaAs NWs that were subjected to a RTA treatment at 250 °C for 20 min for <110> and <100> orientations, respectively. It can be readily observed from these SEM images that the length of nickelide extension into the InGaAs channels strongly depends on the NW widths and no lateral volume expansion is observed in between nickelide segments and the unreacted InGaAs. In addition, the nickelide/InGaAs interface is flat for <110> orientated NWs but is rough for <100> orientated ones. AFM topographical measurements in Figure 1c,d show that the volume expansion is predominant in the vertical <001> direction normal to the substrate surface, and that the NW heights increase from 40 nm in unreacted regions (cyan colored) to around □50-56nm in reacted nickelide regions (red colored). The rough nickelide-InGaAs interface is again observed in the AFM topography for the wider <100> orientated NWs. The origin of these dependencies will be further elucidated with the kinetic and structural characterization of the nickelidation process in following sections.

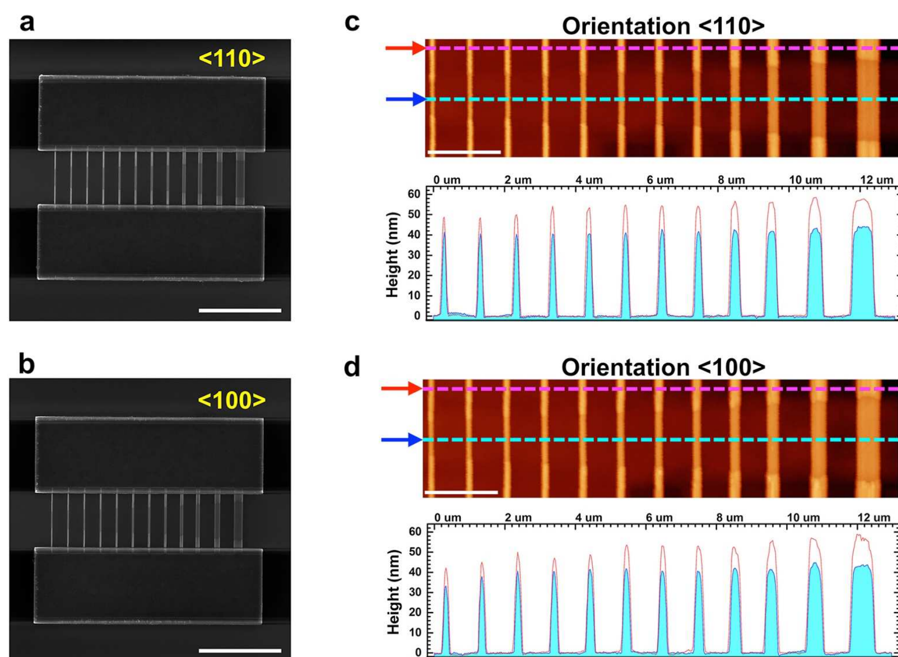

Figure 2. Nickelide formation in InGaAs NW channels. (a, b) SEM images showing the size-dependent and orientation dependent morphologies for nickelide contacts with InGaAs NWs predefined in <110> and <100> orientations, respectively. Scale bars are 5 μm. (c, d) AFM topography plots and their height profiles for nickelide segments (red) and non-reacted InGaAs segments (cyan). Scale bars are 2 μm.

Downloaded on 2018-02-22 to IP 155.69.24.171 address. Redistribution subject to ECS terms of use (see ecsdl.org/site/terms_use) unless CC License in place (see abstract).

Size-Dependent Reaction Kinetics

In order to better understand the nickelide formation mechanism, we extended previous kinetic models for the $NiSi_2$ reactions in Si NWs [6], and took into account the rectangular geometry of our top-down fabricated InGaAs channels and the volume expansion incurred in the reacted regions [14]. As shown in Figure 3, there are three steps during the nickelide growth: ① Ni dissolution across the Ni/nickelide interface, ② Ni diffusion along the formed nickelide segment, and ③ Nickelidation at the fresh nickelide/InGaAs interface.

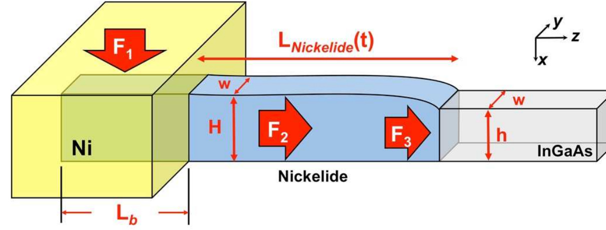

Figure 3. A schematic illustration of the rate-limiting processes involved in nickelidation in InGaAs NW channels with a rectangular cross-section.

By solving the steady-state reactions, the equations under three rate-limiting mechanisms can be expressed as follows [14]:

(1) If the Ni source supply is the rate-limiting step:

$$L_{Nickelide}(t) = k_{dissolve}\left(\frac{1}{H}+\frac{2}{w}\right)L_b P \cdot t \tag{1}$$

(2) If Ni diffusion is the rate-limiting step, and the diffusion is dominant along the surface of the NW channels, i.e. Ni surface-diffusion limited:

$$L_{Nickelide}(t) = \sqrt{4PD_{Ni}\delta \cdot \left(\frac{1}{w}+\frac{1}{H}\right)} \cdot t^{1/2} \tag{2}$$

(3) If Ni diffusion is the rate-limiting step, and the diffusion is through the entire body of the NW channels, i.e. Ni volume-diffusion limited:

$$L_{Nickelide}(t) = \sqrt{2PD_{Ni}} \cdot t^{1/2} \tag{3}$$

(4) If the interfacial reaction is the rate-limiting step:

$$L_{Nickelide}(t) = k_{growth}\frac{h}{H}P \cdot t \tag{4}$$

where, $P = M_{Nickelide} \cdot (C^{eq}_{Ni/Nickelide} - C^{eq}_{Nickelide/InGaAs})/(N_A \cdot \rho_{Nickelide})$ which is a constant. H, h, w are the geometric factors labeled in Figure 3. $k_{dissolve}$ and k_{growth} are the interfacial reaction rate constants for Ni dissolution into nickelide and for nickelide growth at the reaction front with InGaAs, respectively. At these two interfaces, $C^{eq}_{Ni/Nickelide}$ and $C^{eq}_{Nickelide/InGaAs}$ denote the equilibrium Ni concentrations. D_{Ni} is the diffusion coefficient of Ni in the reacted nickelide segment, and δ is the thickness of the high-diffusivity surface layer.

In both the Ni source supply limit and the interfacial kinetic reaction limit, the length of the nickelide segment ($L_{Nickelide}$) is linearly proportional to the annealing time t. This

Downloaded on 2018-02-22 to IP 155.69.24.171 address. Redistribution subject to ECS terms of use (see ecsdl.org/site/terms_use) unless CC License in place (see abstract).

contradicts the experimentally observed $t^{1/2}$ dependence [14], and suggests that the nickelidation process here in the InGaAs channel is dominated by the diffusion of Ni adatoms along the newly formed nickelide segment. The volume-diffusion growth limit is free of geometrical terms, therefore based on our observation that narrower NWs exhibit faster nickelide growth rates (Figure 2), we conclude that Ni adatom mass transport is governed by surface diffusion as precisely described by equation (2) and illustrated in Figure 2.

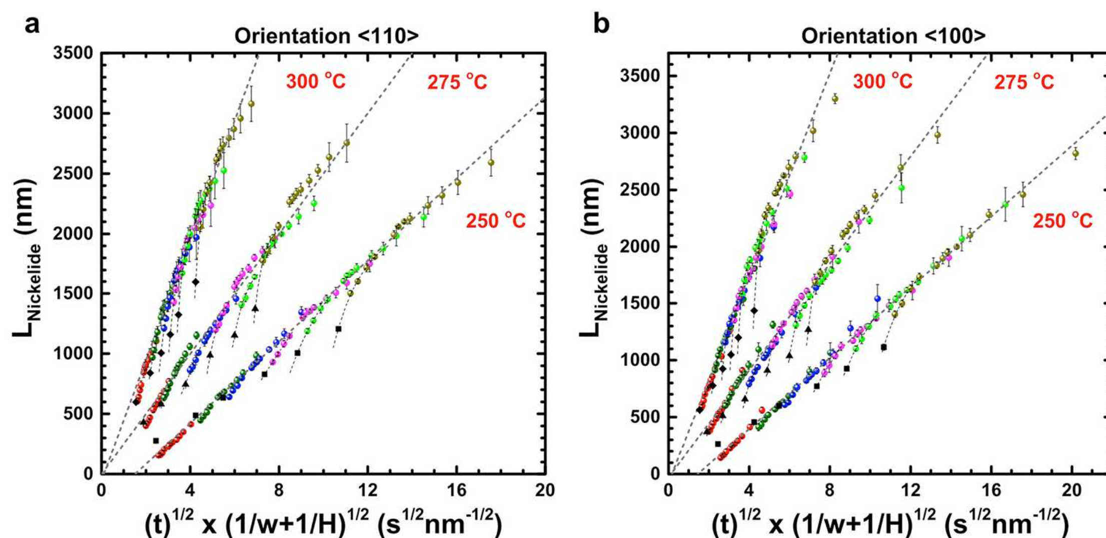

Figure 4. Plots of nickelide segment length in relation to annealing time and geometrical factors, corresponding to <110> and <100> oriented InGaAs NW channels respectively.

To further validate the surface-diffusion limited process, the length of the nickelide segment must follow a linear dependence as a function of $t^{1/2} \times (1/w + 1/H)^{1/2}$ from equation (2) above. This is shown to be the case in Figure 4 at three different reaction temperatures and for both channel orientations. The nonzero intercept of the fitted line with the x-axis for the 250 °C thermal treatment indicates an average incubation behavior of all NWs which is due to the slower nickelide reactions in the planar InGaAs region underneath the Ni contact. However, the nickelide lengths in wider NWs (left-side data points of each data set, color-labeled) fell below the linear trend, indicating a deviation from the surface-diffusion limited model. Interestingly, these deflected data points gradually extend approaching the nickelide lengths in the planar InGaAs films (black squares in Figure 4a,b). In thin films, metal adatoms exhibit volume-like diffusion and as such, larger NWs experience a gradual deviation from surface to volume diffusion.

Atomic Scale Dynamics of Nickelidation in InGaAs Nanowire Cross-sections

To delve deeper into the kinetics and thermodynamics of the phase change of the nickelide contact formation beyond the macroscopic models described above, we utilized the in situ TEM heating technique to capture the atomic scale dynamics of the nickelidation process. Figure 5a,b show the in situ heating stage and the compatible thermal E-chip that has a thin membrane window for placing our specimen. The temperature is controlled by resistive heating and is continuously measured on-chip with

Downloaded on 2018-02-22 to IP 155.69.24.171 address. Redistribution subject to ECS terms of use (see ecsdl.org/site/terms_use) unless CC License in place (see abstract).

a thermocouple. Samples that have Ni contacts on InGaAs NWs were fabricated on a separate substrate (schematic in Figure 5c, with method described in Figure 1) and transferred on top of the membrane window of a thermal E-chip by focused-ion-beam (FIB) milling, lift-out and attachment with a nano-manipulator inside the FIB chamber. On top of the thermal E-chip, we used the FIB to mill an open square on the ceramic membrane and to deposit two Pt posts on opposite sides of the square window (Figure 5d). Subsequently, the specimen lamella was lifted out and transferred on top of the membrane of a thermal E-chip horizontally (schematic in Figure 5e). Finally, this lamella was further thinned to a thickness below 100 nm permitting electron beam transparency.

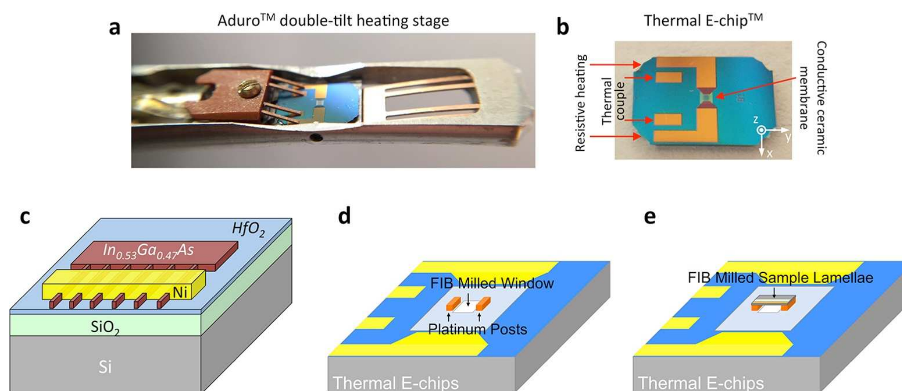

Figure 5. (a, b) photographs of the Protochips Aduro heating stage and its compatible thermal E-chip, respectively. (c-e) Schematics of the process flow (c) representing the FIB process on device substrate and (d-e) representing the transfer process on TEM thermal E-chips.

Solid-State Amorphization and Growth Rate Anisotropy

At temperatures above 180 °C, Ni diffused through the contact interface and reacted with the $In_{0.53}Ga_{0.47}As$ nanowire cross-section to form an amorphous nickelide ($Ni_xIn_{0.53}Ga_{0.47}As$) phase. The reaction onset temperature is reduced by □50 °C compared to planar case and the nickelide phase was amorphous here rather than the crystalline $Ni_2In_{0.53}Ga_{0.47}As$ that is usually obtained at or above 230 °C in the planar case. We also observed that when the temperature was elevated above 375 °C, the amorphized nickelide phase regrew slowly into a crystalline nickelide phase. During this regrowth, further Ni was supplied from the surrounding contact and nickelide poly-crystallites were observed in the first 5 minutes of the reaction. These poly-crystallites gradually transformed into a well-aligned, single-crystalline $Ni_2In_{0.53}Ga_{0.47}As$ that is the thermally stable nickelide phase [15].

At 180 °C, we recorded the layer-by-layer Nickelidation reaction on {111} facets of InGaAs as shown in Figure 6, with ledge movements that were characterized by one of the following mechanisms: (1) Ni flux eliminates one InGaAs atomic layer at a time along a single <112> direction (labeled ① in Figure 6a and schematically shown in Figure 6c), (2) Ni flux eliminates one atomic layer along two opposite <112> directions (labeled ② in Figure 6a and schematically shown in Figure 6d), (3) two ledges that each have a single-layer step height merge into one ledge with double-layer step height

Downloaded on 2018-02-22 to IP 155.69.24.171 address. Redistribution subject to ECS terms of use (see ecsdl.org/site/terms_use) unless CC License in place (see abstract).

(labeled ③ in Figure 6a and schematically shown in Figure 6f), or (4) a double-layer ledge splits into two ledges with single-layer heights (labeled ④ in Figure 6a and schematically shown in Figure 6e) that move independently after splitting. A fixed step height of three or more atomic bilayers is necessary in order to compensate for the shear stress during phase transformations [16], which was not observed in this experiment implying the absence of shear stress during this nickelide reaction.

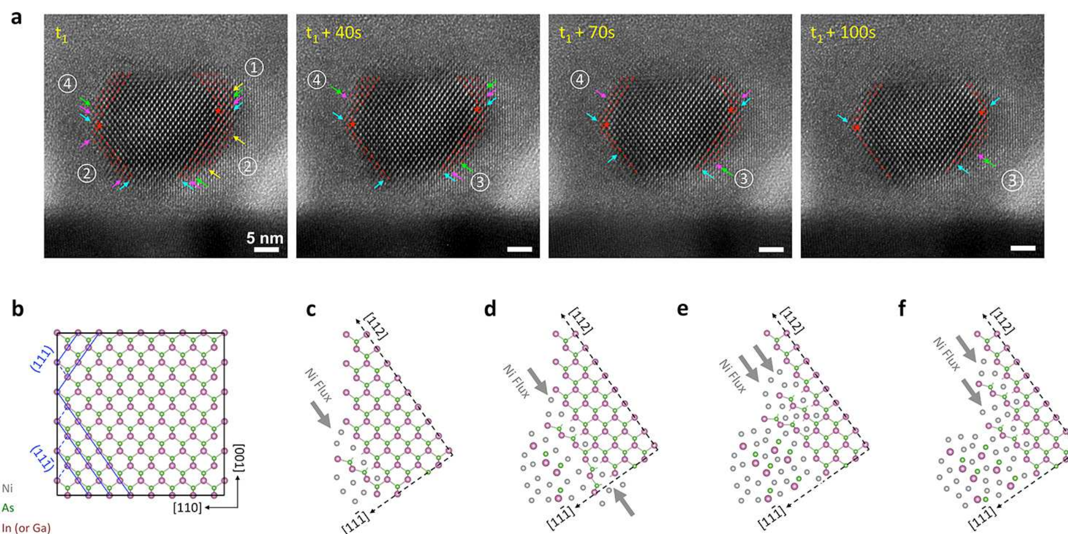

Figure 6. (a) High-resolution TEM (HRTEM) sequences and (b-f) reconstructed lattice structures that illustrate the ledge formation and movement mechanisms at atomic resolution.

Influence of Contact Interface on Nickelide Morphologies and Reaction Kinetics

During the study of the nickelide reaction in InGaAs NW cross-sections, we noticed that the quality of the interface between Ni and InGaAs NW played an important role in both the nickelide morphologies and reaction kinetics. Therefore, we prepared two types of specimens to illustrate these differences.

In the first set of specimens, we intentionally introduced a thin (1−2 nm) surface oxide layer on the InGaAs NWs prior to Ni deposition (schematic in Figure 7a). This oxide layer prevented the intermixing of Ni and InGaAs upon Ni deposition. The as-fabricated InGaAs NW had a square cross-section with an edge width of □15 nm (Figure 7b). Upon annealing the specimen *in-situ* inside the TEM chamber, the Ni diffused through the interfacial oxide layer and along the surface of the InGaAs NW, quickly forming an amorphous nickelide shell of uniform thickness. Then, the nickelide shell grew evenly along the top and side surfaces of the nanowire (Figure 7b, t = 4 min), even in regions that voids exist in between Ni and the nanowire sidewall due to shadowing effects during the metal deposition process. Following this shell formation (Figure 7b, t = 8 min), the nickelide reaction further extends to the bottom region of the nanowire that forms the InGaAs/HfO_2 interface, gradually isolating the crystalline InGaAs core from the HfO_2 substrate (Figure 7b, t = 12 min) by an intermediate amorphous nickelide region.

Downloaded on 2018-02-22 to IP 155.69.24.171 address. Redistribution subject to ECS terms of use (see ecsdl.org/site/terms_use) unless CC License in place (see abstract).

This process creates stepped interfaces that gradually eliminates the non-{111} facets and result in a rhomboidal core of crystalline InGaAs (Figure 7b, t = 24 min).

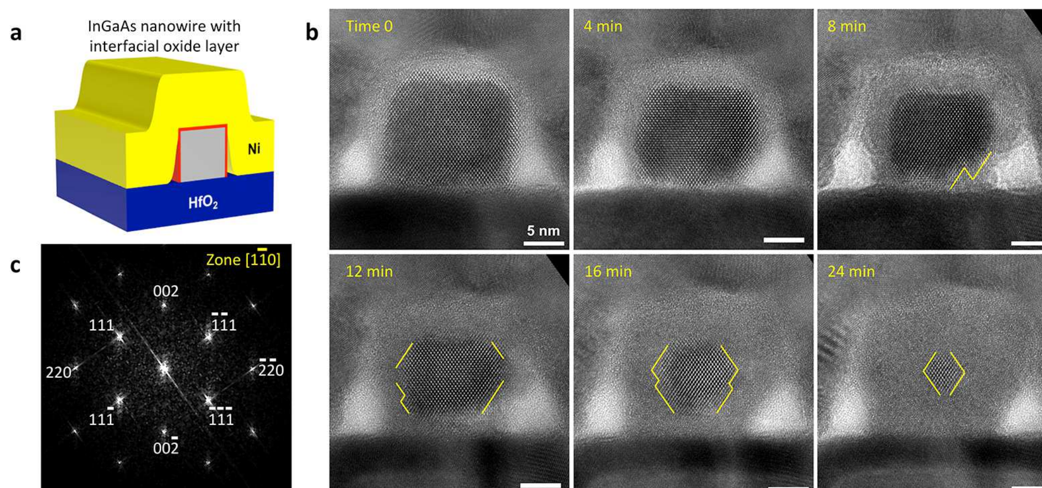

Figure 7. (a) Schematic of Ni contacting with an InGaAs NW cross-section that has a surface oxide layer. (b) HRTEM sequences during the *in situ* heating experiment at 180 °C. (c) Fast Fourier transform (FFT) image of the corresponding nanowire cross-section.

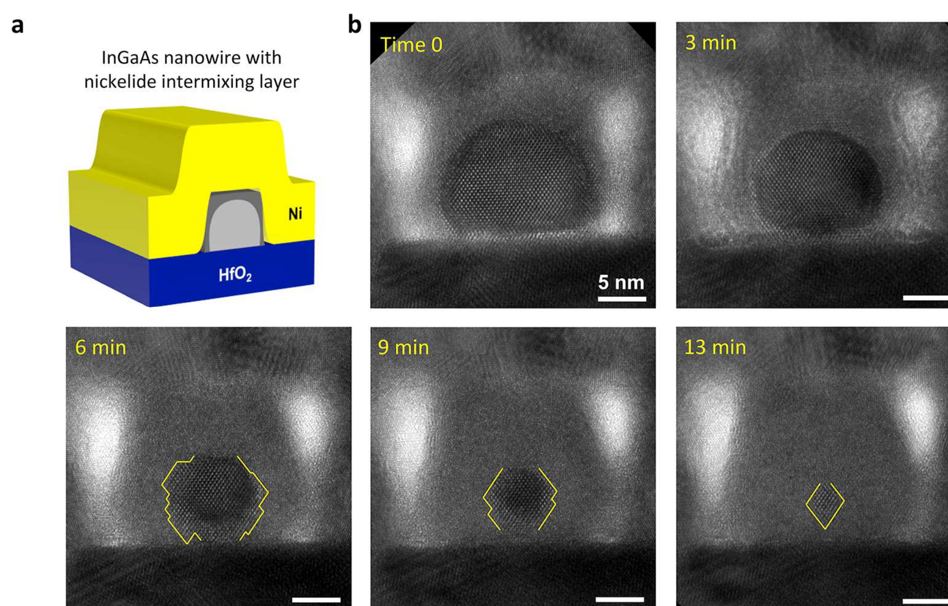

Figure 8. (a) Schematic of Ni contacting with an InGaAs NW cross-section with an intermixing layer in between. (b) HRTEM sequences during the *in situ* heating experiment at 180 °C.

In the second set of specimens, the direct deposition of metal on the InGaAs NW surface leads to the formation of an intermixed layer due to the latent heat exchange

Downloaded on 2018-02-22 to IP 155.69.24.171 address. Redistribution subject to ECS terms of use (see ecsdl.org/site/terms_use) unless CC License in place (see abstract).

when the metal atoms condense from the vapor phase to the solid phase. Further heating the sample to 180 °C *in-situ* in the TEM, we observe the nickelide reaction at the interface between InGaAs and HfO_2 at the bottom of the NW, which is facilitated by Ni diffusing through the existing intermixing layer making the InGaAs core even more rounded (Figure 8b, $t = 3$ min). As the reaction continues, many small facets are observed at 6 min and gradually develop into several {111} types of facets at 9 min. Eventually, the crystalline InGaAs core becomes a rhomboidal shape after 13 min, very similar to that of Figure 7b.

These two types of interfaces between Ni and InGaAs NWs were found to directly influence the reaction kinetics. To capture these differences, we modified the kinetic models that were based on metal diffusion in the cross-section of a rectangular nanowire to depict the reaction in the radial direction of the nanowire's cross-section (Figure 9a). For simplicity we assumed an infinite Ni source supply, a cylindrical shape of the NW, and a fixed outer perimeter L (no volume expansion after nickelidation).

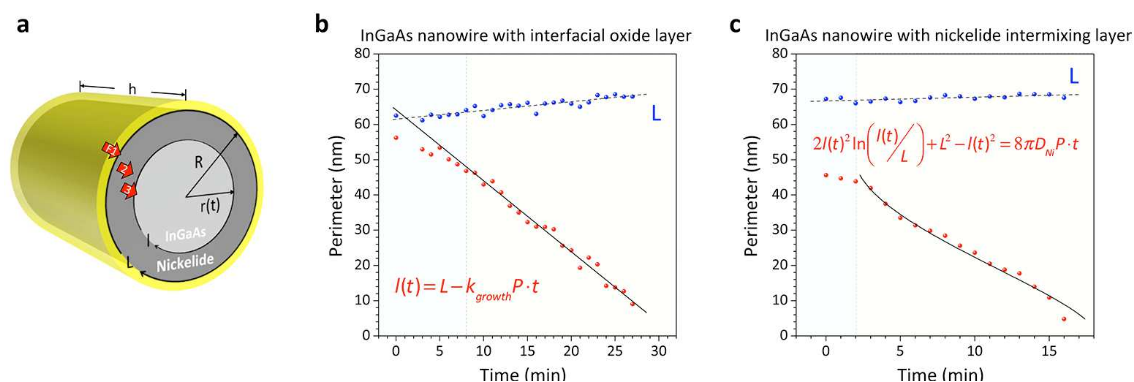

Figure 9. (a) Modeling the metallic contact formation in the radial direction of a nanowire channel. (b, c) Plots of the inner and outer perimeters for these two types of specimens with different contact interfaces between Ni and InGaAs NW.

We found that for the first type of specimen with an interfacial oxide layer in between Ni and InGaAs (as shown in Figure 7), the inner perimeter, l, obeys a linear dependence on time (Figure 9b) that follows a behavior that is consistent with *F3* being the rate-limiting step, i.e., kinetically limited growth at the nickelide/InGaAs interface. For the second type of specimen that had the intermixing layer in between Ni and InGaAs (Figure 9c), the characteristic shape of the plot of l includes rapid decays at both the beginning and the very end with an approximately linear segment in between, following a diffusion/mass-transport limited process (F2). This change from kinetically limited to a mass-transport limited nickelide formation is due to the differences in the interfacial properties between Ni and InGaAs. In the second type of specimen, an intermixing layer readily forms upon Ni deposition, resulting in a rounded InGaAs cross-section (Figure 8b, t = 0). The rounded surfaces introduce many kink sites on small facets of the nickelide/InGaAs interface, facilitating the reaction rate at these interfaces and thereby accelerating the kinetics of the reaction. The rate of arrival of Ni adatoms to the reaction interface became the rate-limiting step and therefore, the nickelide reaction became mass-transport/thermodynamically limited.

Downloaded on 2018-02-22 to IP 155.69.24.171 address. Redistribution subject to ECS terms of use (see ecsdl.org/site/terms_use) unless CC License in place (see abstract).

Atomic Scale Dynamics of Nickelidation along InGaAs Channel Directions

After formation of the nickelide underneath the Ni contact, further nickelide extension into the channel is expected. To study the lateral extension of nickelide into the channel, we prepared our *in-situ* heating TEM specimens with a similar FIB-milling and lamellae-transferring procedure to that shown in Figure 5, but the lamellae was cut along the channel direction.

Figure 10 provides an overview of the interfacial profile between InGaAs NW and the reacted nickelide phase after applying the *in-situ* heating at 320 °C. Here, we deduced the nickelide phase as $Ni_2In_{0.53}Ga_{0.47}As$ by cross examining the lattice constant (from FFT patterns) with known values for this phase [16]. From the diffraction patterns of the two phases across the interface, we found that the interfacial atomic planes followed the $In_{0.53}Ga_{0.47}As$ (111) || $Ni_2In_{0.53}Ga_{0.47}As$ (0001) alignment, in agreement with our earlier *ex-situ* studies [14]. In the following sections, we present a deeper understanding of the interfacial atomic arrangements, ledge formation and movement behaviors deduced from the *in-situ* microscopy studies.

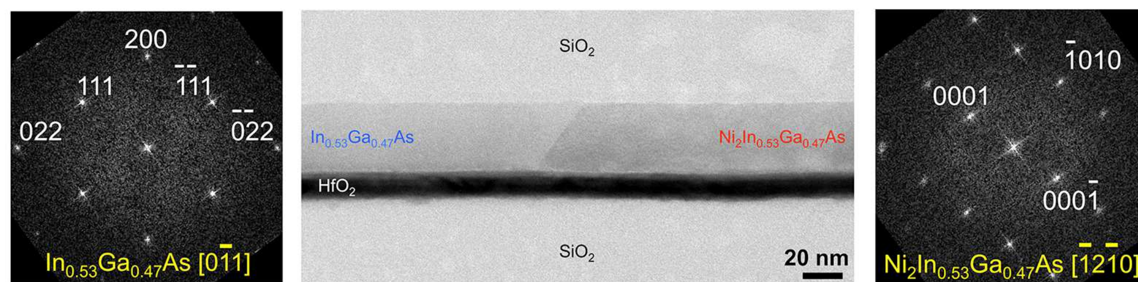

Figure 10. TEM image of the InGaAs/Nickelide interface showing a slanted interfacial profile.

Ledge Nucleation and Propagation Behaviors

We recorded the nickelidation process with high-resolution TEM (HRTEM) at ×1M magnification and extracted the time-resolved frames (shown in Figure 11) from the digital video. To the best of our knowledge, this is the first *in-situ* observation of the solid-state reaction between metal and III–V nanowires with atomic resolution that clearly resolves ledge formation and movement.

We found that the $Ni_2In_{0.53}Ga_{0.47}As$ ledges nucleate as a train of single-bilayers near the top surface of the nanowire channel, which can be observed in each frame of Figure 11. These single-bilayer ledges were under biaxial tensile stresses from inside the interfacial plane ($In_{0.53}Ga_{0.47}As$ (111) || $Ni_2In_{0.53}Ga_{0.47}As$ (0001)) due to a lattice mismatch of 5.5%, and a uniaxial compressive stress in the direction that is perpendicular to the interfacial plane due to nickelide volume expansion of 34.2% [14]. In principle, these two effects add up the compression of $Ni_2In_{0.53}Ga_{0.47}As$ lattice in the out-of-plane directions. The very thin (<80 nm) TEM sample lamellae, prepared by FIB in this study, facilitates lateral volume expansion that is perpendicular to the channel, reducing the overall influence of volume expansion on the interfacial stress. Figure 11 shows that these single bilayer ledges moved freely at the beginning on the $Ni_2In_{0.53}Ga_{0.47}As$ (0001)

Downloaded on 2018-02-22 to IP 155.69.24.171 address. Redistribution subject to ECS terms of use (see ecsdl.org/site/terms_use) unless CC License in place (see abstract).

surface along the [10-10] direction from the top surface to the center region of the nanowire. Shortly thereafter, the compressive stress was released by generating misfit dislocations that hindered the fast movement of these nucleated single-bilayers. These newly generated misfit dislocations were captured in the time frame of 9”49”’, under two different single-bilayer ledges that are marked with cyan and green colored arrows. Once a misfit dislocation is formed, the propagation speed of a single-bilayer ledge decreased, and another single-bilayer ledge growth can reach the first single bilayer, merging into a double-bilayer. Thereafter, the ledge moved with a double-bilayer height that coupled with a misfit dislocation of $\boldsymbol{b}$ = 2c/3[0001]. Even though two double-bilayer ledges could instantly merge into a quadruple-layer ledge and then separate into independent double-bilayer ledges again in the following movements (e.g., time duration of 14”05”’–19”38”’, the ledges related to the two labeled dislocations toward the bottom of the images), a double-bilayer ledge remained stable once coupled with a dislocation and never split into two single-bilayers in all the following time sequences. This indicates that the double-bilayer is the unit height for a moving $Ni_2In_{0.53}Ga_{0.47}As$ ledge after the generation of a misfit dislocation at the reacting $Ni_2In_{0.53}Ga_{0.47}As/In_{0.53}Ga_{0.47}As$ interface.

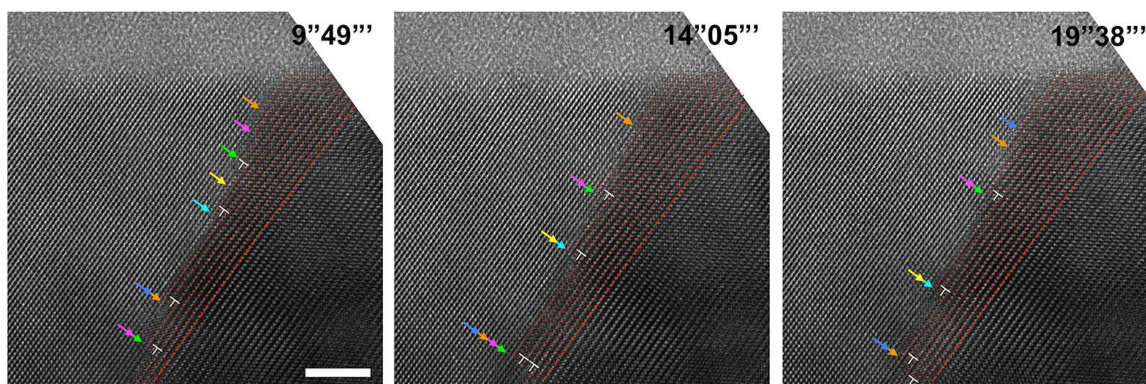

Figure 11. HRTEM sequences showing the ledge formation at the top-surface of nanowire channel and ledge propagations into the nanowire body. Scale bar is 5 nm.

Interfacial Disconnections and Atomic Models

The behaviors of ledge nucleation and movement observed in the nickelidation process are significantly different from the preceding studies on metallic processes in elemental semiconductors, such as in Si nanowires. When nickel silicide forms in Si nanowire channels, $NiSi_2$ with cubic lattice structure is the immediate adjacent phase to pristine Si and it has a lattice constant very close to that of Si [4]. Therefore, the $NiSi_2$ phase grew epitaxially on the coherent $Si/NiSi_2$ interface by forming ledges of a single-bilayer height. However, during phase transformation in the $In_{0.53}Ga_{0.47}As/Ni_2In_{0.53}Ga_{0.47}As$ system, the large lattice mismatch results in a misfit dislocation in every second atomic bilayer in $Ni_2In_{0.53}Ga_{0.47}As$ (corresponding to every third atomic bilayers in $In_{0.53}Ga_{0.47}As$, as will be discussed in detail below). The ledges of $Ni_2In_{0.53}Ga_{0.47}As$ had a unit height of a double-bilayer and coupled with the misfit dislocations. This type of interface that comprises both ledge and misfit dislocation is generally referred to as an interfacial “disconnection” [17-18].

Downloaded on 2018-02-22 to IP 155.69.24.171 address. Redistribution subject to ECS terms of use (see ecsdl.org/site/terms_use) unless CC License in place (see abstract).

Figure 12 shows two magnified HRTEM images of the interfacial disconnections. From time t_1 in Figure 12, a clear correlation can be seen in between three layers of $In_{0.53}Ga_{0.47}As$ lattice planes (marked with yellow dashed lines) and two layers of $Ni_2In_{0.53}Ga_{0.47}As$ lattice planes (marked with red dashed lines). Therefore, there exists a misfit dislocation with a Burgers vector ***b*** = a/3[111] for every three atomic-layers of $In_{0.53}Ga_{0.47}As$, where a = 5.87 Å is the lattice constant of the $In_{0.53}Ga_{0.47}As$ (zinc-blende). $Ni_2In_{0.53}Ga_{0.47}As$ has a hexagonal lattice with lattice constants of a = 3.93 Å and c = 5.10 Å [14]. The Burgers vector defined above is equivalent to 2c/3[0001]. At time t_2 in Figure 12, we observe the same behavior, where the unit height of ledges is a double-bilayer.

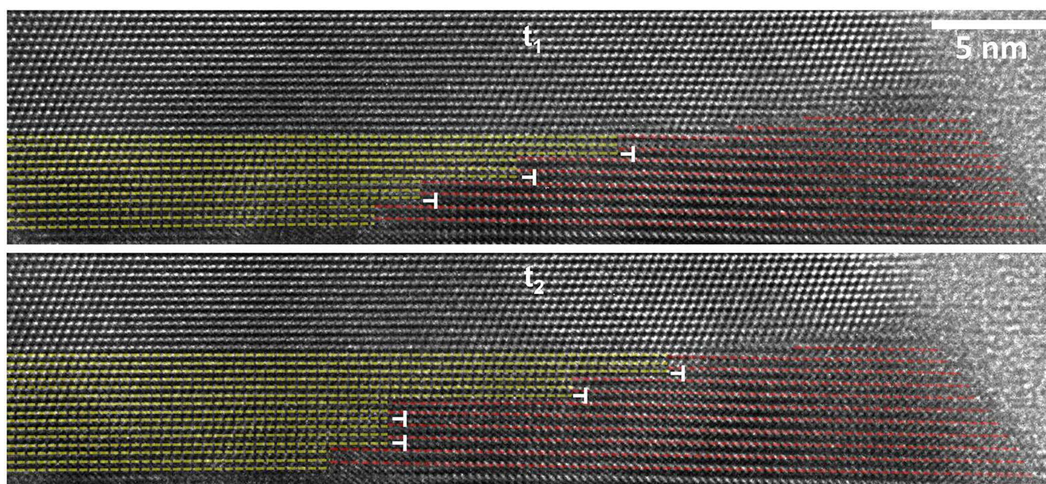

Figure 12. HRTEM images of an even closer look at the InGaAs/Nickelide interface, demonstrating the interfacial disconnections.

An insightful understanding of the interfacial disconnection and the ledge movement behavior is achieved with the atomic models that we developed in order to construct the crystal structures at the $In_{0.53}Ga_{0.47}As/Ni_2In_{0.53}Ga_{0.47}As$ interface. It starts with the basic lattice structures of zinc-blende $In_{0.53}Ga_{0.47}As$ and hexagonal $Ni_2In_{0.53}Ga_{0.47}As$ as shown in Figure 13a. As in a typical fcc structure, the atomic planes arrange in a A-B-C-A-B-C. . . manner (shown in Figure 13b) along the [111] direction of the $In_{0.53}Ga_{0.47}As$ crystal. Due to the nature of the simple hexagonal lattice of $Ni_2In_{0.53}Ga_{0.47}As$, which is different from typical hexagonal-close-packed (hcp) stacking, the atomic planes arrange in an A-A-A. . . manner, along the [0001] direction of $Ni_2In_{0.53}Ga_{0.47}As$ crystal. Therefore, during the $In_{0.53}Ga_{0.47}As$ phase transformation into $Ni_2In_{0.53}Ga_{0.47}As$, the atomic bilayers need to glide in each atomic plane and transform from A-B-C. . . type of stacking into A-A-A. . . type of stacking. Here, we depict the gliding behavior in Figure 13c,d by simplifying one atomic-bilayer into a lattice plane. From a top-view of the lattice planes (Figure 13c), the top lattice plane has three optional gliding directions in order to overlap with the bottom lattice plane, i.e., 1/6[11-2], 1/6[1-21], and 1/6[-211], corresponding to three Shockley partial dislocations (also referred to as Shockley partials). From a side-view of the lattice planes (Figure 13d), three lattice planes need to glide collectively with each lattice plane along one of the three Shockley partials in order to eliminate shear stress during phase transformation [19]. This is a prerequisite for phase transformation as no external shear

Downloaded on 2018-02-22 to IP 155.69.24.171 address. Redistribution subject to ECS terms of use (see ecsdl.org/site/terms_use) unless CC License in place (see abstract).

stress was applied to the NW. Consequently, a group of three (or multiples of three) atomic bilayers in the $In_{0.53}Ga_{0.47}As$ crystal will glide collectively to have three Shockley partials cancel each other. This triple-bilayer in the $In_{0.53}Ga_{0.47}As$ crystal has a height of 3d(111) = 10.17 Å which is nearly equivalent to the height of double-bilayer ledge (2d(0001) = 10.20 Å) in the $Ni_2In_{0.53}Ga_{0.47}As$ crystal accommodated with residual strain ≤0.3%. This also introduces one misfit-dislocation for each double-bilayer ledge. Finally, atomic reconstruction at the disconnection interface is shown in Figure 13e, and both the single-bilayer nucleus and the double-bilayer ledges are illustrated in the schematic.

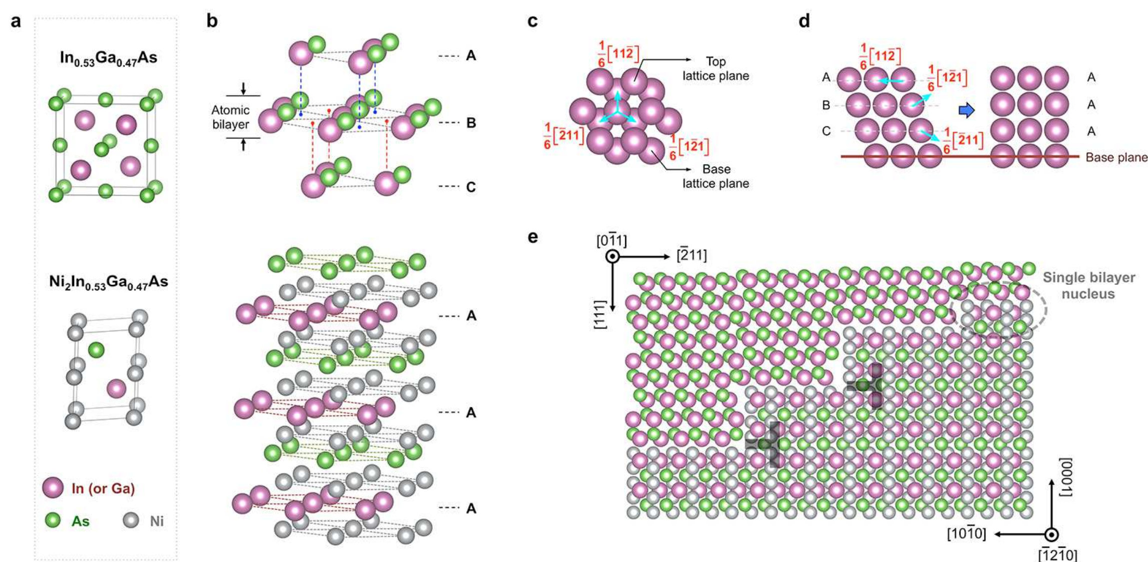

Figure 13. Atomic models that reveal the formation of interfacial disconnections during $In_{0.53}Ga_{0.47}As$ to $Ni_2In_{0.53}Ga_{0.47}As$ phase transformation.

Electrical Properties of InGaAs Nanochannels with Ni Contact

We fabricated InGaAs FinFETs on insulator on Si substrate by a wafer bonding process that has been discussed in the prior section [13]. A representative SEM image is shown in the insert of Figure 14 for the as-fabricated InGaAs FinFETs with the Nickelide contact at the planar region at both ends. Transistor performance of these devices was measured after a 5 min RTA at 200 °C in forming gas (H_2/N_2 mixture). This RTA process is believed to stabilize the intermixing layer between Ni and InGaAs planar source/drain regions, without introducing significant nickelide growth. The transfer characteristics of a representative device with 10 FinFET channels with a single Fin perimeter of 60 nm and a channel length of 390 nm, are shown in Figure 14. The current was normalized by the perimeter of the Fins, as measured by TEM, and by the number of channels. This device exhibited an I_{on} = 18 μA/μm at V_{DS} = 0.5 V and $V_{GS} - V_T$ = 0.5 V, where the threshold voltage V_T = 0.78 V was extracted by the linear extrapolation of the $I_{DS} - V_{GS}$ at the maximum slope (peak transconductance, g_m). An inverse subthreshold slope (SS^{-1}) of 165 mV/dec and a maximum current sweep ratio (I_{max}/I_{low}) of 3.2×10^6 at V_{DS} = 0.05 V were observed. The interface quality for these FinFET devices on Si compares well to those on InP [20] and lags behind some others with Al_2O_3 interfacial gate dielectric layers [21]. Further optimization of the HfO_2/InGaAs interface and reduced Fin widths were

Downloaded on 2018-02-22 to IP 155.69.24.171 address. Redistribution subject to ECS terms of use (see ecsdl.org/site/terms_use) unless CC License in place (see abstract).

found to result in lower SS^{-1}. The gate leakage was as low as 10^{-6} μA/μm for all the V_{DS} biases used in this study up to $V_{DS} = 1$ V. The on-current of these devices was limited by the series contact resistance due to the Schottky barrier nature between the Ni S/D contacts and the undoped InGaAs, which was also responsible for the increment of I_{DS} in the negative V_{GS} region from hole transport. Therefore, further modifications are needed for the annealing process of nickelidation in the nanochannels as discussed in the last subsection of this paper.

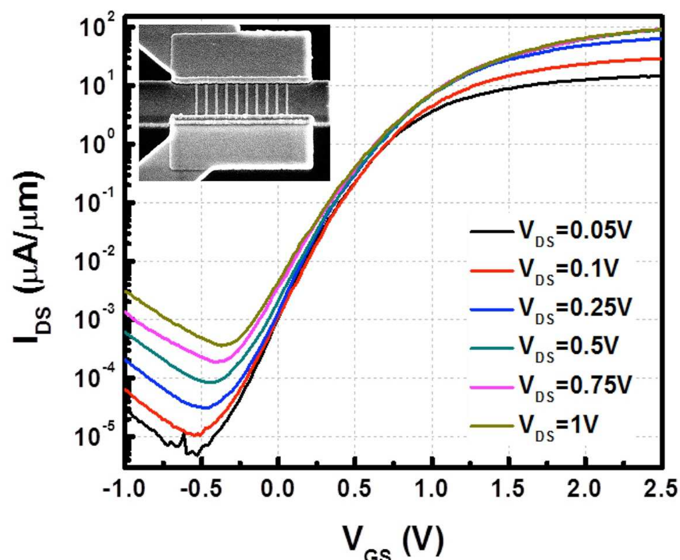

Figure 14. Measured transfer characteristics of a group of InGaAs NWs on Si with perimeter of 60 nm and channel length of 390 nm for different V_{DS} biases.

Strain-Induced Band-Edge Energy Shift at the Nickelide/InGaAs Interface

The interface between InGaAs and nickelide experiences stresses that modify the contact and charge injection propertied. The in-plane ($\varepsilon_{//}$) and out-of-plane ($\varepsilon_{\perp}$) strains are plotted as a function of distances from the nickelide/InGaAs interface in Figure 15a. The measured inter-plane spacing from the FFT patterns was used to calibrate the $\varepsilon_{//}$ and $\varepsilon_{\perp}$ by comparing these values with those measured far from the interface. It can be seen that nickelidation process exerted a quasi-hydrostatic compressive stress to the InGaAs channel, as both the $\varepsilon_{//}$ and $\varepsilon_{\perp}$ showed negative values ($\sim -2\%$) at the nickelide/InGaAs interface. The $\varepsilon_{\perp}$, caused by the compression from nickelide volume expansion, gradually relaxed far from the interface. The $\varepsilon_{//}$, caused by interfacial lattice mismatch, exhibits several fluctuations before decreasing to zero. From the trend of $\varepsilon_{//}$, the compressive strain at the nickelide/InGaAs interface should be below 3%. However, this value is smaller than 5.6% (the theoretical lattice mismatch between $In_{0.53}Ga_{0.47}As$ and $Ni_2In_{0.53}Ga_{0.47}As$), which is likely to be relaxed by the three free surfaces of the InGaAs channel and the saw-tooth like steps present at the nickelide/InGaAs interface. Under this quasi-hydrostatic compressive stress, the band structure of $In_{0.53}Ga_{0.47}As$ is significantly modified, and the strain-induced shift in band-edge energies can be calculated using well-

Downloaded on 2018-02-22 to IP 155.69.24.171 address. Redistribution subject to ECS terms of use (see ecsdl.org/site/terms_use) unless CC License in place (see abstract).

known elastic theory that incorporates deformation potentials [22]. Figure 15b shows the calculated band-edge energies as a function of distance from the nickelide/InGaAs interface (detailed calculations in [14]). The heavy hole (E_{hh}) and light hole (E_{lh}) bands split under the compressive strain with the E_{hh} slightly higher than E_{lh}, which is different from the conventional cases of band anti-crossing under uniaxial and biaxial stresses. The E_g gradually increases from the relaxed center of the channel (0.75 eV) toward the strained interface with a peak value of □1.26 eV at the interface. Such an increase of E_g could result in a much larger electron effective mass and a significant reduction of the injection velocities in ultrascaled semiconductor channels. A larger stress-induced band-gap of InGaAs may be detrimental for ohmic contact formation with InGaAs channels due to the increased Schottky barrier height (SBH). Possible strategies to mitigate these effects may include contact engineering that can allow for the formation/piling of higher In composition (or higher dopants) in InGaAs near the contact region to compensate the stress effects and to lower E_g (or to reduce the SBH thickness).

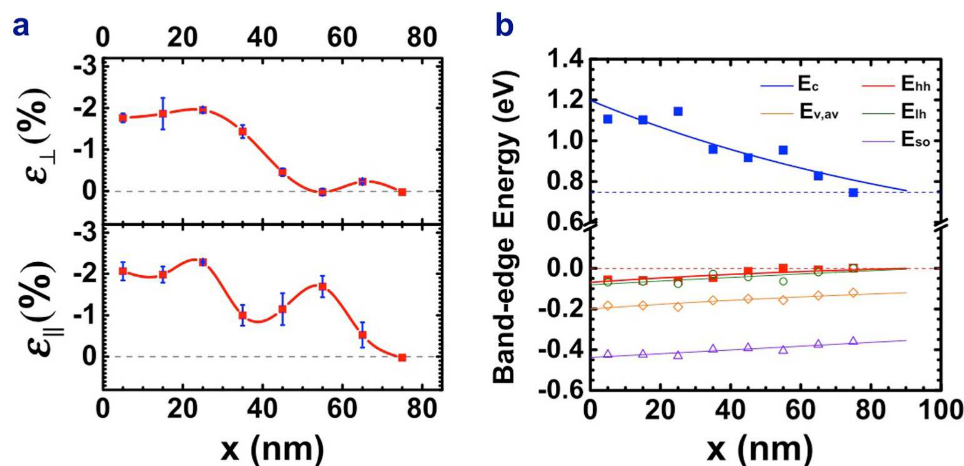

Figure 15. (a) Out-of-plane and in-plane strains of InGaAs as a function of distance from the interface, calculated by comparing the inter-plane spacing from FFT diffraction patterns with the unstrained one. (b) The calculated band-edge energies as a function of distance along x-axis based on elastic theory that incorporates deformation potentials.

Proposed Ohmic Contact Engineering by Solid-State Regrowth

One possible method to mitigate the strain-induced band-gap opening is to employ a solid-phase regrowth (SPR) technique to the metallic contact formation. The schematic for this process is shown in Figure 16, with Pd/Si/Ti metal stacks deposited on the cross-section of InGaAs NW channels. The SPR contact metallization process can include two steps: (1) In the first step, Pd reacts with InGaAs NW at a low temperature (~ 100 °C), to form a Pd-InGaAs alloy. (2) In the second step, the excess Pd reacts with the Si layer at higher temperatures (> 300 °C) to form a $PdSi_2$ alloy and Si diffuses through this layer to interface with the Pd-InGaAs alloy. At the same time, due to the instability of the Pd-InGaAs alloy at high temperatures, the more stable silicide phase takes over the Pd atoms from the Pd-InGaAs alloy, resulting in a SPR of InGaAs near the NW surface with an epitaxial and single-crystalline phase. During this regrowth step, the dopant (Si) will be

Downloaded on 2018-02-22 to IP 155.69.24.171 address. Redistribution subject to ECS terms of use (see ecsdl.org/site/terms_use) unless CC License in place (see abstract).

introduced at the surface in the regrown InGaAs layer, which will eventually reduce the width of Schottcky barrier and result in an ohmic-like contact.

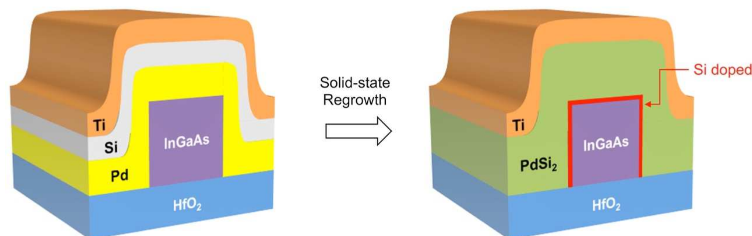

Figure 16. Schematics of the solid-state regrowth concept in InGaAs nanochannels.

Acknowledgments

This work was performed at the Center for Integrated Nanotechnologies (CINT), a U.S. Department of Energy Office of Basic Energy Sciences user facility at Los Alamos National Laboratory (Contract DE-AC52-06NA25396) and Sandia National Laboratories (Contract DE-AC04-94AL85000) through a CINT user proposal. The authors would like to acknowledge discussions with Drs. Nan Li, Wei Tang, Jinkyoung Yoo and Ms. Ren Liu, as well as discussions and technical support from Anthony R. James, Douglas V. Pete, Denise B. Webb and Willard Ross of Sandia National Laboratories. S.A.D. thanks NSF support for R.C. under DMR-1503595, and partially from ECCS-1351980.

References

1. S. A. Dayeh, D. P. Aplin, X. Zhou, P. K. Yu, E. T. Yu and D. Wang, *small*, **3**(2), 326-332 (2007).
2. S. A. Dayeh, D. Susac, K. L. Kavanagh, E. T. Yu and D. Wang, *Nano letters*, **8**(10), 3114-3119 (2008).
3. F. Léonard and A. A. Talin, *Nature Nanotechnology*, **6**(12), 773-783 (2011).
4. W. Tang, S. A. Dayeh, S. T. Picraux, J. Y. Huang and K.-N. Tu, *Nano Letters*, **12**(8), 3979-3985 (2012).
5. W. Tang, S. T. Picraux, J. Y. Huang, A. M. Gusak, K.-N. Tu and S. A. Dayeh, *Nano Letters*, **13**(6), 2748-2753 (2013).
6. W. Tang, B.-M. Nguyen, R. Chen and S. A. Dayeh, *Semiconductor Science and Technology*, **29**(5), 054004 (2014).
7. R. Chen, B.-M. Nguyen, W. Tang, Y. Liu, J. Yoo and S. A. Dayeh, *Applied Physics Letters*, **110**(21), 213103 (2017).
8. J. A. Del Alamo, *Nature*, **479**(7373), 317-323 (2011).
9. M. Abraham, S.-Y. Yu, W. H. Choi, R. T. Lee and S. E. Mohney, *Journal of Applied Physics*, **116**(16), 164506 (2014).
10. L. Czornomaz, M. El Kazzi, M. Hopstaken, D. Caimi, P. Mächler, C. Rossel, M. Bjoerk, C. Marchiori, H. Siegwart and J. Fompeyrine, *Solid-State Electronics*, **74**, 71-76 (2012).
11. Ivana, Y. Lim Foo, X. Zhang, Q. Zhou, J. Pan, E. Kong, M. H. Samuel Owen and Y.-C. Yeo, *Journal of Vacuum Science & Technology B*, **31**(1), 012202 (2013).

Downloaded on 2018-02-22 to IP 155.69.24.171 address. Redistribution subject to ECS terms of use (see ecsdl.org/site/terms_use) unless CC License in place (see abstract).

12. P. Shekhter, S. Mehari, D. Ritter and M. Eizenberg, *Journal of Vacuum Science & Technology B*, **31**(3), 031205 (2013).
13. X. Dai, B. M. Nguyen, Y. Hwang, C. Soci and S. A. Dayeh, *Advanced Functional Materials*, **24**(28), 4420-4426 (2014).
14. R. Chen and S. A. Dayeh, *Nano letters*, **15**(6), 3770-3779 (2015).
15. R. Chen, K. L. Jungjohann, W. M. Mook, J. Nogan and S. A. Dayeh, *Nano Letters*, **17**(4), 2189-2196 (2017).
16. R. Chen and S. A. Dayeh, *Small*, DOI: 10.1002/smll.201604117, (2017).
17. J. Hirth, *Metallurgical and Materials Transactions A*, **25**(9), 1885-1894 (1994).
18. J. P. Hirth, *Journal of Physics and Chemistry of Solids*, **55**(10), 985-989 (1994).
19. N. Li, S. K. Yadav, J. Wang, X.-Y. Liu and A. Misra, *Scientific Reports*, **5**, 18554 (2015).
20. H.-C. Chin, X. Gong, L. Wang, H. K. Lee, L. Shi and Y.-C. Yeo, *IEEE Electron Device Letters*, **32**(2), 146-148 (2011).
21. J. Gu, X. Wang, H. Wu, J. Shao, A. Neal, M. Manfra, R. Gordon and P. Ye, *Electron Devices Meeting (IEDM)*, 27.6.1, (2012).
22. C. G. Van de Walle, *Physical review B*, **39**(3), 1871 (1989).

Downloaded on 2018-02-22 to IP 155.69.24.171 address. Redistribution subject to ECS terms of use (see ecsdl.org/site/terms_use) unless CC License in place (see abstract).